(Received 20 December 2024, Accepted 3 March 2025, Scheduled 17 March 2025)

A Frequency Selective Rasorber with Ultra-Wideband Switchable Transmission/Reflection and Two-Sided Absorption

Liangzhen Lin, Jianqiong Zhang*, Liangzhu Li, Xiangqiang Li, and Qingfeng Wang

Southwest Jiaotong University, Chengdu 610031, China

ABSTRACT: A novel switchable frequency selective rasorber (FSR), featuring dual wideband absorption bands and an ultra-wide passband that can be switched to a reflective band, is proposed in this work. This design incorporates a lossy layer and a three-layer reconfigurable frequency selective surface (FSS). An ultra-wideband transmission can be achieved through the lossy layer by means of circular spiral resonators. The switchable function is utilized by a reconfigurable FSS with PIN diodes. Simulation results confirm the FSR's broad absorption from 1.44 to 2.39 GHz (49.6%) and from 5.45 to 6.64 GHz (19.7%). It also achieves an extensive passband with a 1-dB bandwidth of 47.78% (3.17∼5.16 GHz) in the absorption-transmission-absorption (A-T-A) mode, which is the widest transmission band in existing designs. The passband is converted into a reflection band in the absorption-reflection-absorption (A-R-A) mode, showcasing the FSR's switchable characteristics. To validate these simulation outcomes, a prototype measuring 300×300 mm is constructed and measured.

1. INTRODUCTION

Frequency selective rasorbers (FSRs) have garnered considerable attention due to their out-of-band absorption and in-band transmission performance attributing to the combination of absorber and frequency selective surface (FSS). FSRs can be categorized in accordance with the relative location of the transmission and absorption bands as follows: 1) above the absorption band (referred to as A-T) [1–3]; 2) below the absorption band (T-A) [4, 5]; and 3) within the absorption band (A-T-A) [6–11]. Great development of FSRs has been made, facilitating the exploration of novel designs and applications in secure communication systems [12–16]. The aforementioned devices can provide a transmission band, but the transmission window cannot be closed, making them vulnerable to interference. Therefore, switchable FSRs with dynamic control, have attracted more concern [17–21]. There are lots of functionalities that reconfigurable FSRs have developed, such as wideband absorption, anomalous reflection, focusing, beam-steering, electro-optical tuning, and sensing [22–24]. However, existing switchable FSRs often suffer from narrow transmission bands or limited switchability, which restricts their practical utility. Moreover, with the application of broadband antenna and multi-antenna integration, the passband width has also become the key direction of FSR research, the wide-band transmission characteristic could be highly beneficial for high-speed data transfer. It can also be applied in satellite communication, enabling more efficient communication between satellites and ground stations. Therefore, the research targeting the broadening of bandwidth has received significant research interest.

A novel switchable FSR with switchable function and an ultra-wide transmission band is proposed. As its vital component, a lossy layer based on circular spiral resonators and a square loop is introduced to realize an ultra-wide transmission band and absorption bands around. Subsequently, a three-layer reconfigurable FSS is designed underneath to provide the same transmission window as the lossy layer and the conversion between transmission and reflection. Thus, the FSR can be switched between A-T-A and A-R-A modes. The simulation and measurement results have validated the design methodology.

2. DESIGN AND ANALYSIS OF THE FSR

The overall model is established based on the structure depicted in Fig. 1. The FSR is composed of a lossy layer, a three-layer reconfigurable FSS, and an air layer between each two substrate structures.

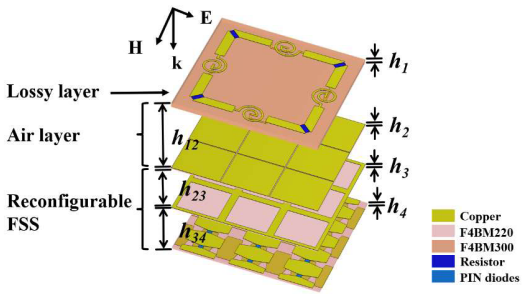

FIGURE 1. The structure of the proposed switchable FSR. The geometric parameters of the structure are as follows: $h_1 = 1$, $h_2 = 0.2$, $h_3 = 0.2$, $h_4 = 0.5$, $h_{12} = 12$, $h_{23} = 3$, $h_{34} = 2$. (Units: mm).

* Corresponding author: Jianqiong Zhang (qilinxing@163.com).

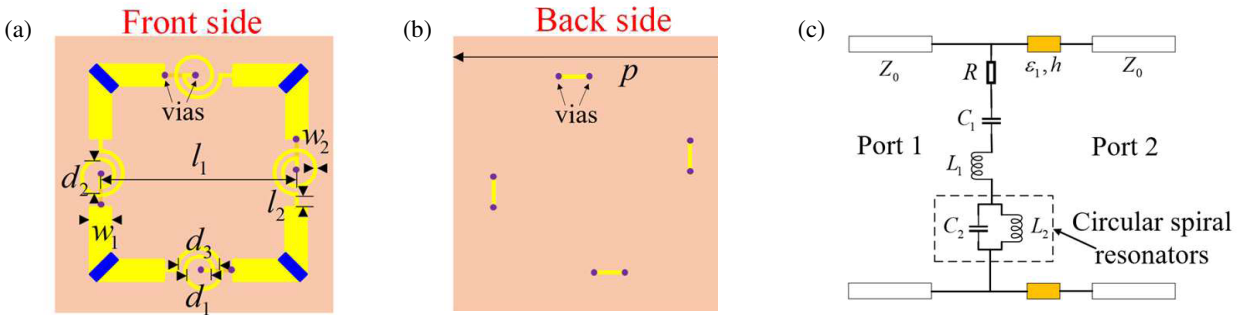

FIGURE 2. The structure and equivalent circuit model of the lossy layer. (a) Front side. (b) Bottom side (c) Equivalent circuit model. The geometric parameters of the structure are as follows: $p = 30$, $w_1 = 2$, $w_2 = 0.4$, $d_1 = 2.2$, $d_2 = 3.3$, $d_3 = 4.4$, $l_1 = 23$, and $l_2 = 0.8$. (Units: mm) Circuit parameters are as follows: R = 370 Ω, $C_1 = 0.0453$ pF, $C_2 = 0.0467$ pF, $L_1 = 42.73$ nH, $L_2 = 37.41$ nH.

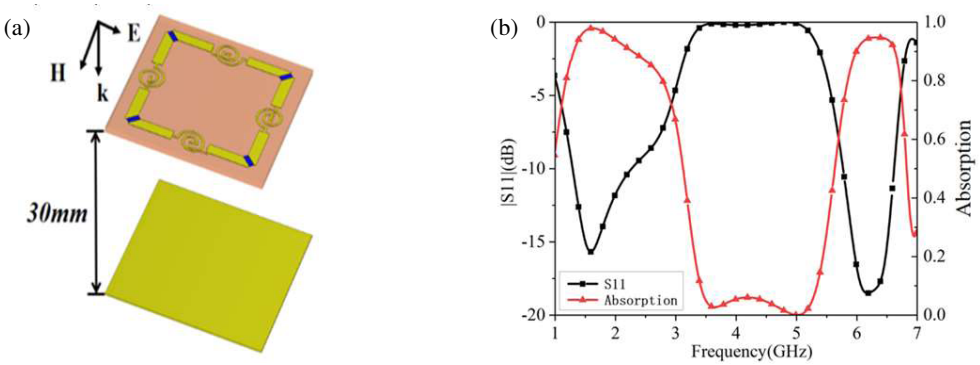

FIGURE 3. The structure and simulated results of lossy layer with metal reflective plate. (a) The structure. (b) The simulated results.

2.1. Analysis of the Lossy Layer

As illustrated in Fig. 2, a 0.035-mm-thick copper structure is printed on the F4BM300 ($\varepsilon_r = 3.0$, $\tan\delta = 0.001$) dielectric material. The lossy layer consists of a square loop with lumped resistors positioned on the corner to obtain broadband impedance matching and wave absorption at both ends of the transmission band, and circular spiral resonators in the center of the four sides to offer high inductance and low capacitance. The value of the lumped resistors is 240 Ω. There are vias in the center of the resonators and in the loop, respectively, connected by a wire on the back side.

A simplified equivalent circuit model (ECM) is proposed in Fig. 2, corresponding to the incident polarization. The circular spiral resonator can be modeled as an LC parallel resonator, which is equivalent to an L_2C_2 parallel circuit, and the loop is equivalent to the L_1. C_1 represents the capacitance between the square loops of adjacent units, and R represents the total equivalent resistance. To validate the absorptive performance, a metallic plate is placed 30 mm behind it, which is depicted in Fig. 3(a). The geometric structure is simulated in CST Studio Suite (CST). Fig. 3(b) shows that the structure is fully reflective in 3.28∼5.25 GHz. Moreover, two absorption bands with absorption above 90% are achieved from 1.29 to 2.29 GHz and 5.76 to 6.6 GHz.

The transmittance, reflectivity, and absorption of the FSR structure are calculated through the transmission and reflection coefficients between the two ports, denoted by T, R, and A, respectively, which are calculated by the formula Absorption = $1 - |S_{11}|^2 - |S_{21}|^2$.

2.2. Analysis of the Reconfigurable FSS

The mechanism of the reconfigurable FSS can be explained through the two-port network illustrated in Fig. 4. The frequency response of the bandpass FSS is mainly determined by the first resonance and last resonance. Therefore, the N-order bandpass filter circuit can be segmented into three sections: L_1-C_1' parallel, L_N-C_N' parallel, and the equivalent two-port network between them.

By cascading the three components, the $ABCD$ matrix of the N-order bandpass filter circuit is derived

$$\begin{bmatrix} A & B \\ C & D \end{bmatrix} = \begin{bmatrix} 1 & 0 \\ \frac{1}{Z_1'} & 1 \end{bmatrix} \times \begin{bmatrix} A' & B' \\ C' & D' \end{bmatrix} \times \begin{bmatrix} 1 & 0 \\ \frac{1}{Z_N'} & 1 \end{bmatrix}, \quad (1)$$

where A', B', C' and D' represent the $ABCD$ matrix of the two-port network in the dashed box. Z_1' and Z_N' are the impedance of the first resonator and last resonator, respectively, and the expressions are as follows:

$$Z_1' = \frac{j\omega L_1}{1 - \omega^2 L_1 C_1'}, \quad (2)$$

$$Z_N' = \frac{j\omega L_N}{1 - \omega^2 L_N C_N'}. \quad (3)$$

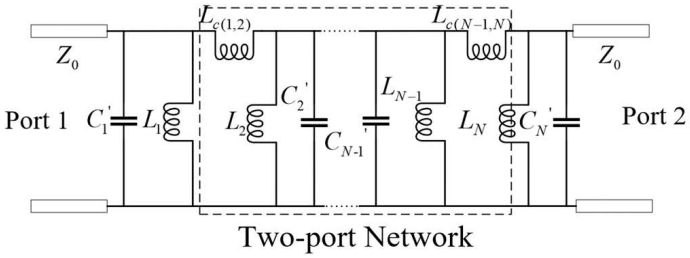

FIGURE 4. Equivalent two-port network of multilayer FSS.

The resonance frequencies of the two resonators are as follows:

$$f_1' = \frac{1}{2\pi}\sqrt{\frac{1}{L_1 C_1'}}, \tag{4}$$

$$f_N' = \frac{1}{2\pi}\sqrt{\frac{1}{L_N C_N'}}. \tag{5}$$

The S-parameters are obtained by the transformation of the $ABCD$ matrix:

$$|S_{11}| = \left|\frac{A' + \frac{B'}{Z_0} - C'Z_0 - D' + K_{1a}}{A' + \frac{B'}{Z_0} + C'Z_0 + D' + K_{1b}}\right|, \tag{6}$$

$$|S_{22}| = \left|\frac{-A' + \frac{B'}{Z_0} - C'Z_0 + D' + K_{2a}}{A' + \frac{B'}{Z_0} + C'Z_0 + D' + K_{2b}}\right|, \tag{7}$$

where

$$K_{1a} = \frac{B'\left(Z_1' - Z_N' - Z_0\right) - Z_0\left(D'Z_1' + A'Z_N'\right)}{Z_1' Z_N'}, \tag{8}$$

$$K_{2a} = \frac{B'\left(Z_N' - Z_1' - Z_0\right) - Z_0\left(D'Z_1' + A'Z_N'\right)}{Z_1' Z_N'}, \tag{9}$$

$$K_{1b} = K_{2b} = \frac{B'(Z_1' + Z_N' + Z_0) + Z_0(D'Z_1' + A'Z_N')}{Z_1' Z_N'}. \tag{10}$$

When the parameters of the left and right components in Fig. 4 are symmetrical, a standard N-order bandpass frequency selection surface is represented, resulting in a bandpass response centered around that frequency. However, when the parameters are asymmetrical, the two parallel resonators resonate at different frequencies, leading to a frequency separation between the two resonant frequencies. In this situation, Z_N' is approximated to be 0 in the vicinity of f_1', and Z_1' is approximated to be 0 in the vicinity of f_N'. As a consequence, when the FSS operates in the asymmetric configuration, $|S_{11}|$ becomes equal to 1, representing a fully reflective state.

Therefore, the two resonant frequencies can be controlled by adjusting the capacitance of the parallel resonances. When the resonant frequencies are the same, the FSS achieves a transmissive characteristic, and when the resonant frequencies are far away from each other, it obtains a reflective characteristic, so as to realize the switching of a transmissive state to a fully reflective state.

The reconfigurable FSS consists of a three-layer structure: A capacitive square patch layer, an inductive grid layer, and a switching layer that consists of a metal strip with hourglass-shaped gap loaded with PIN diodes, as shown in Fig. 5. F4BM220 ($\varepsilon_r = 2.2$, $\tan\delta = 0.001$) is used as the dielectric layer for the reconfigurable FSS, and the unit cell of the FSS measures $10 \times 10\,\text{mm}^2$. The PIN diodes are SMP 1320-040 LF with the following equivalent parameters: 1) ON-state: $L_{\text{PIN}} = 0.45\,\text{nH}$ and $R_{\text{ON}} = 0.75\,\Omega$; 2) OFF-state: $L_{\text{PIN}} = 0.45\,\text{nH}$ and $C_{\text{OFF}} = 0.23\,\text{pF}$. Each layer is separated by an air layer.

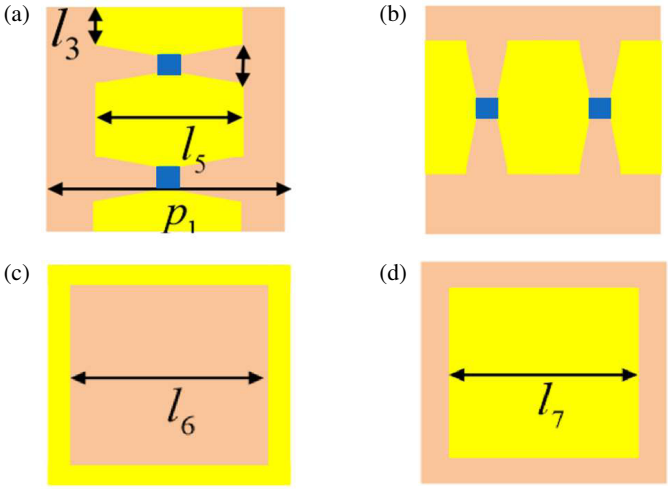

FIGURE 5. The structure of the the reconfigurable FSS. (a) Front side of the switching layer. (b) Back side of the switching layer. (c) The middle layer. (d) The top layer. The geometric parameters of the structure are as follows: $p_1 = 10$, $l_3 = 1.2$, $l_4 = 2$, $l_5 = 7$, $l_6 = 8.5$, $l_7 = 9.8$. (Units: mm).

The equivalent circuit model of the reconfigurable FSS is shown in Fig. 6(a). The square patch can be modeled by a capacitance C_3, and the grip is defined as an inductance L_3. C_4 models the gap between the metal strip, and C_5 represents the capacitive coupling effects between the unit cell. The ON-state PIN diode is represented with a series of L_{PIN} and R_{ON}, and the OFF-state PIN diode is represented with a series of L_{PIN} and C_{OFF}. When the diodes are off, since the impedance is relatively small, typically only several ohms, the effect can be neglected. Consequently, capacitance C_1 and diode parasitic capacitance

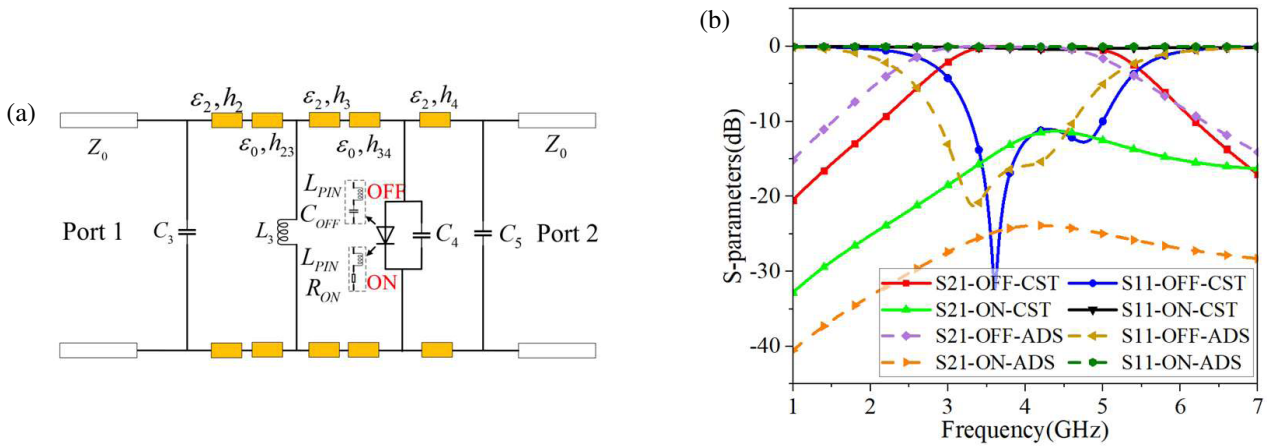

FIGURE 6. The equivalent circuit model and simulated results of the reconfigurable FSS. (a) The equivalent circuit model. (b) The simulated results. Circuit parameters are as follows: $C_3 = 0.265$ pF, $C_4 = 0.0348$ pF, $C_5 = 0.0592$ pF, $L_3 = 2.67$ nH, $L_4 = 9.54$ nH.

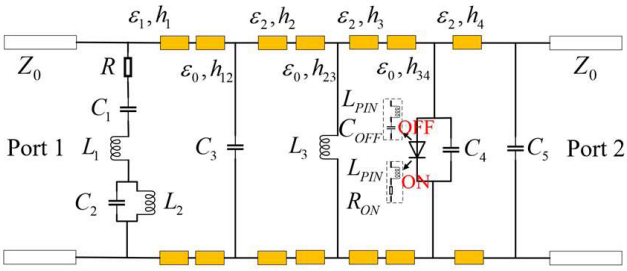

FIGURE 7. The equivalent circuit model of the proposed switchable FSR.

C_{OFF} are in parallel. By adjusting C_1, so that $C_1 + C_{OFF} = C_2$, the structure of the circuit becomes symmetrical, and wave-transparency can be realized. Conversely, when the diodes are on, the parasitic inductance and positive resistance are sufficiently small to be approximated as a short circuit, thus short-circuiting C_1 and impacting reflective characteristics to the entire structure. The design facilitates the passband switchable characteristics of the reconfigurable FSS.

The frequency response of the reconfigurable FSS is illustrated in Fig. 6(b). The S-parameters of the equivalent circuit model are analyzed using Keysight Advanced Design System (ADS), which are basically consistent with the full-wave simulation of CST. When the diodes are off, a 1-dB transmission band is achieved from 3.17 to 5.16 GHz. However, when the diodes are on, the transmission coefficient decreases to -10 dB, and the reflection coefficient exceeds -1 dB across the 1 to 7 GHz range.

2.3. Analysis of Proposed FSR

Based on the proposed FSR, a simplified equivalent circuit model is proposed in Fig. 7. Furthermore, each substrate layer is modeled by a short section of transmission line with length h and characteristic impedance of $Z_T = Z_0/\sqrt{\varepsilon_r}$, where $Z_0 = 377\,\Omega$ represents the impedance of free space, and ε_r denotes the relative permittivity of the substrate layer.

The simulated results of the two modes are shown in Fig. 8. The results indicate that the FSR has the capability to switch between two modes. In the A-T-A mode, the FSR exhibits an ultrawide transmission band in the frequency range from 3.02 to 5.17 GHz by offering a fractional bandwidth of 52.5% (2.15 GHz), and two absorption bands with absorption over 80% are from 1.44 to 2.39 GHz and from 5.45 to 6.64 GHz. In the A-R-A mode, the transmission band turns to reflection band with reflection coefficient over 1 dB, and the overall transmission coefficient is lower than -10 dB.

The S-parameters and absorption of the switchable FSR under different resistances are shown in Fig. 9. With the resistance R increasing from 120 Ω to 370 Ω, S_{21} is almost unaffected. However, S_{11} decreases; therefore, the bandwidth of the absorption bands is broadened. The maximum relatively absorption bandwidths are obtained at $R = 370\,\Omega$.

The S-parameters and absorption of the switchable FSR under different side lengths of the rectangular patch are shown in Fig. 10. When l_7 increases from 9.2 mm to 9.8 mm, the higher resonant frequency of S_{21} shifts to the lower frequency; therefore, the upper absorption band forms and gets broader. Usually when the transmission band gets wider, the absorption in the direction of the widening will be squeezed and narrowed. In order to broaden the operating bandwidth, including the transmission band and absorption band for further research, more complex structures, such as multi-layer designs [25, 26], convoluted structures [27, 28], and 2.5D/3D structures [27, 29], are usually required.

The simulated S-parameters of the FSR under different incident angles in TE and TM waves are depicted in Fig. 11(a) and Fig. 11(b). As the incidence angle is varied from 0° to 40°, with the increase in incident angle, the passband maintains high transmittance. Despite the deteriorations, the FSR continues to exhibit significant transmission/reflection switching functions. Fig. 11(c) shows that the FSR has stable absorption characteristics up to an incidence angle of 30°, indicating relatively stable performance under oblique incidence.

In order to highlight the superior performance of the proposed FSR, the comparison with other reported designs is

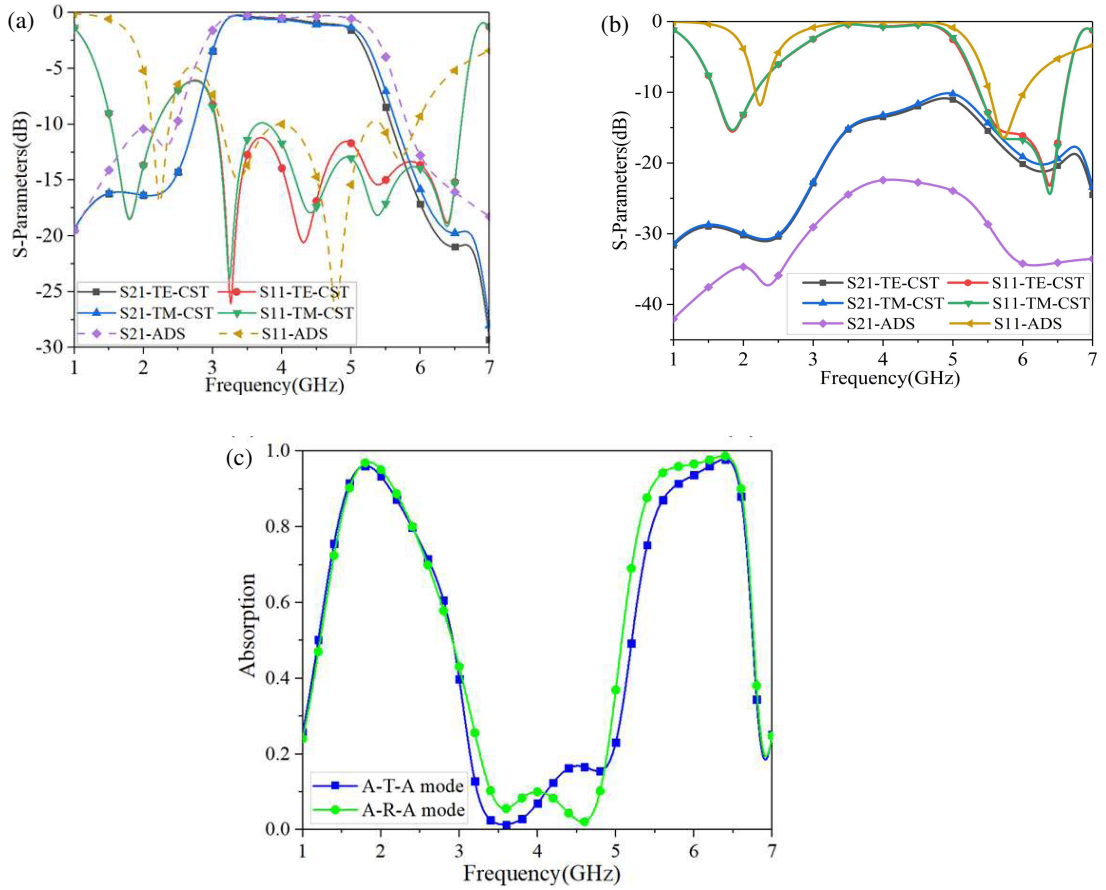

FIGURE 8. S-parameters and absorption of the switchable FSR in A-T-A mode and A-R-A mode. (a) S-parameters in A-T-A mode. (b) S-parameters in A-R-A mode. (c) Absorption.

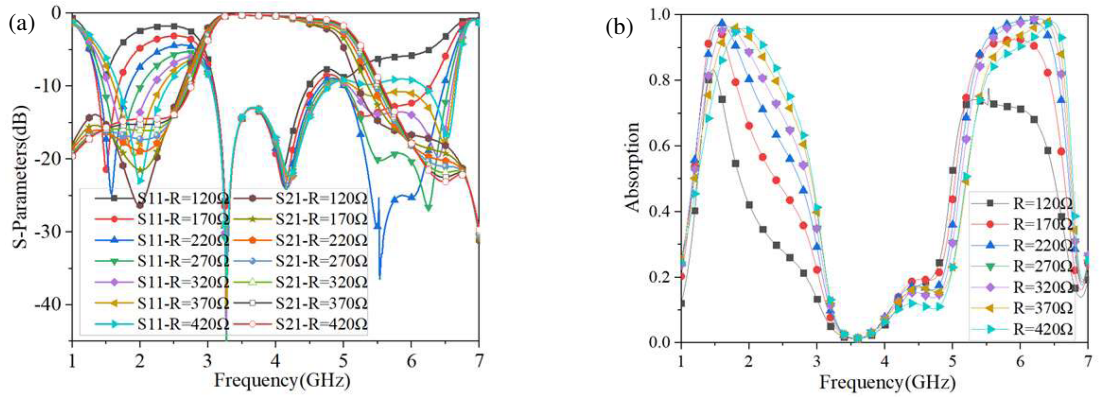

FIGURE 9. S-parameters and absorption of the switchable FSR under different resistance R. (a) S-parameters. (b) Absorption.

shown in Table 1. Compared with the reported FSR, it is concluded that the proposed switchable FSR offers the widest transmission band with two-sided absorption in switchable FSRs.

3. EXPERIMENTAL RESULTS AND DISCUSSIONS

A 300×300 mm prototype consisting of 9×9 units is fabricated and tested, as shown in Fig. 12(a) and Fig. 12(b). The lumped resistors with the package type of 0603 are soldered in the lossy layer, and PIN diodes SMP 1320-040 LF are welded on both sides of the switching layer. Five nylon studs are placed on each side to fix the device, and PMI foam is interspersed between the layers to provide structure strength and spacing control. Copper strips are added as bias lines to realize electrical connection, and each DC bias network has a total voltage of 48.85 V. GHA0118A-11 UWB horn antennas with operating frequency of 1–18 GHz are used as transmitting and receiving antennas.

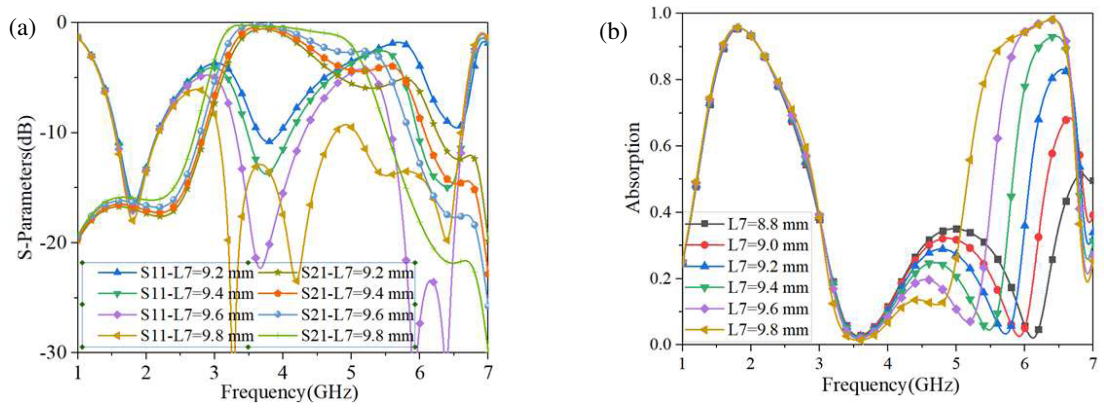

FIGURE 10. S-parameters and absorption of the switchable FSR under different side length of the rectangular patch l_7. (a) S-parameters. (b) Absorption.

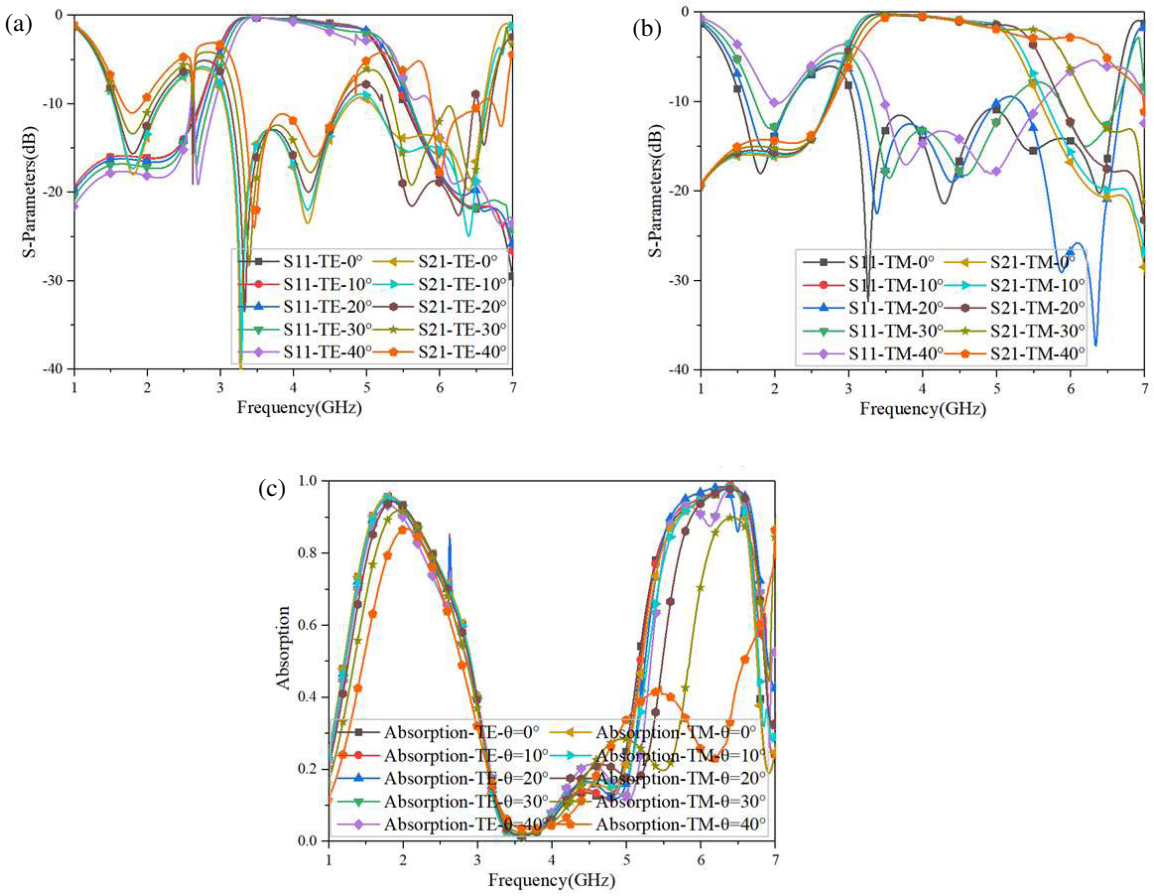

FIGURE 11. S-parameters and absorption of the switchable FSR for the oblique incidence. (a) S-parameters in TE polarization. (b) S-parameters in TM polarization. (c) Absorption.

KEYSIGHT E5071C vector network analyzer is used for testing. When measuring the transmission coefficient, the horn antennas are placed at both sides of the prototype of the FSR, and while measuring the coefficient, the horn antennas are placed on the same side of the prototype, symmetrically. The switchable function is realized by whether the power is on or off.

The measured S-parameters of the proposed FSR structure at normal incidence are shown in Fig. 12(c). The measurement results show that: when the diodes are off, a 1-dB passband of 3.02∼4.86 GHz is realized, and the reflection coefficient within 1.52∼2.16 GHz and 2.94∼6.56 GHz is below −10 dB; when the diodes are on, a 1-dB reflection band is achieved in 3.22∼4.76 GHz and the transmission coefficient reduced to less than −10 dB in 1∼7 GHz, which demonstrates an ultra-wide passband and switchable performance. The measured absorption of the proposed FSR structure at normal incidence is

TABLE 1. Comparison with reported frequency selective rasorbers.

Ref.	Type	Passband	Absorption band	Thickness (mm)	Pol.
[2]	A-T	9.00∼12.63 GHz (33.5%)/−1 dB	3.88∼7.63 GHz (65.2%)	10.5(0.38λ_C)	Dual
[16]	A-T-A	7.81∼11.78 GHz (40.53%)/−1 dB	3.67∼6.80 GHz (60.2%)/13.74∼15.31 GHz (10.8%)	9.8(0.32 λ_C)	Dual
[20]	A-T-A/ A-R-A	3.67∼3.93 GHz (6.8%)/−3 dB	2.37∼3.23 GHz (30.7%)/4.09∼6.63 GHz (47.4%)	9.1(0.12 λ_C)	Dual
[29]	A-T-A	14.3∼16.27 GHz (12.89%)/−3 dB	4.2∼12.6 GHz (97.67%)/18.7∼22.5 GHz (20.87%)	8.3(0.24λ_C)	Dual
[30]	A-T	7.5∼10.2 GHz (30.5%)/−3 dB	2.4∼6.2 GHz (65.2%)	14(0.20λ_C)	Dual
[31]	A-T-A/ A	3.5∼4.8 GHz (31.3%)/−1 dB	0.85∼2.93 GHz (110.1%)/5.4∼7.47 GHz (32.2%)	39(0.54λ_C)	Single
[32]	A-T-A	7.66∼11.76 GHz (42.2%)/−1 dB	3.53∼7.16 GHz (81.6%)/12.55∼17.19 GHz (20.8%)	12.2(0.39λ_C)	Dual
This FSR	A-T-A/ A-R-A	Sim:3.17∼5.16 GHz (47.78%)/−1 dB Mea:3.02∼4.86 GHz (46.7%)/−1 dB	Sim:1.44∼2.39 GHz (49.6%)/5.45∼6.64 GHz (19.7%) Mea:1.51∼2.34 GHz (43.1%)/5.56∼6.44 GHz (14.7%)	18.9(0.25 λ_C)	Dual

Note: λ_C is the wavelength of the first center absorption frequency.
The relative bandwidth is placed in brackets and is calculated as relative bandwidth = bandwidth/center frequency.
The level of the absorption band is 80%, expect for [2, 32] which is 90%.

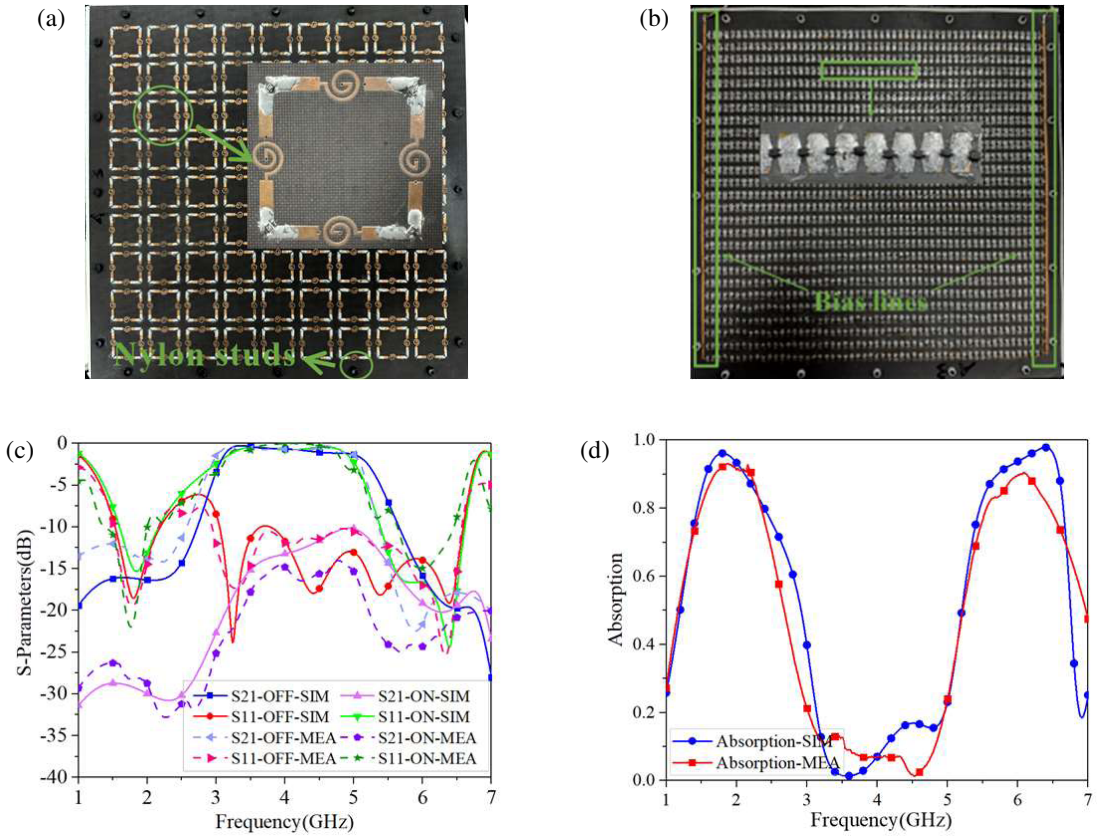

FIGURE 12. The structure and measurement results of the fabricated prototype. (a) Top view of the lossy layer. (b) Bottom view of the switching layer. (c) S-parameters (d) Absorption.

shown in Fig. 12(d), which is calculated from the measured S-parameters and the formula Absorption $= 1 - |S_{11}|^2 - |S_{21}|^2$. The absorption bands are from 1.51 to 2.34 GHz and from 5.56 to 6.44 GHz. The deviations between measurement and simulation results may be due to scattering in directions other than normal incidence, surface roughness, and measurement errors. The experimental results are in good agreement with the simulation ones.

4. CONCLUSION

In conclusion, this study introduces a switchable frequency selective rasorber (FSR) that possesses an ultra-wide transmission band. The innovative design incorporates circular spiral resonators and lumped resistors within the lossy layer, complemented by PIN diodes strategically positioned on both sides of the underlying layer of the reconfigurable FSS. This configuration endows the device with a broad transmission window and dual absorption bands, as well as the capability to transition seamlessly between the absorption-transmission-absorption (A-T-A) mode and absorption-reflection-absorption (A-R-A) mode. The proposed FSR shows two distinct absorption bands along with an ultra-wide transmission band and excellent switchability. These characteristics make the device particularly suitable for complex applications in radar cross-section (RCS) reduction and electromagnetic interference (EMI) shielding, and the wide-band transmission can help to meet the requirements for high-capacity data channels.

ACKNOWLEDGEMENT

This work was supported by the Fundamental Research Operation Funds of the Central Universities of China under Grant 2682023ZTPY059.

REFERENCES

[1] Chen, Q., M. Guo, Z. Sun, D. Sang, and Y. Fu, "Polarization-independent frequency-selective rasorber with a broadened absorption band," *AEU — International Journal of Electronics and Communications*, Vol. 96, 178–183, Nov. 2018.

[2] Guo, M., Q. Chen, T. Bai, K. Wei, and Y. Fu, "Wide transmission band frequency-selective rasorber based on convoluted resonator," *IEEE Antennas and Wireless Propagation Letters*, Vol. 19, No. 5, 846–850, May 2020.

[3] Liao, K., S. Liu, X. Zheng, X. Zhang, X. Shao, and X. Kong, "An ultra-wide passband frequency-selective rasorber with high transmission," *Microwave and Optical Technology Letters*, Vol. 64, No. 11, 1911–1916, Jul. 2022.

[4] Hong, T., S. Guo, W. Jiang, and S. Gong, "Highly selective frequency selective surface with ultrawideband rejection," *IEEE Transactions on Antennas and Propagation*, Vol. 70, No. 5, 3459–3468, May 2022.

[5] Yi, B., P. Liu, G. Li, and Y. Dong, "Design of miniaturized and ultrathin absorptive/transmissive radome with wideband absorbing property," *Microwave and Optical Technology Letters*, Vol. 58, No. 8, 1870–1875, Aug. 2016.

[6] Xia, J., J. Wei, Y. Liu, Y. Zhang, S. Guo, C. Li, S. Bie, and J. Jiang, "Design of a wideband absorption frequency selective rasorber based on double lossy layers," *IEEE Transactions on Antennas and Propagation*, Vol. 68, No. 7, 5718–5723, Jul. 2020.

[7] Xiu, X., W. Che, W. Yang, Y. Han, and Q. Xue, "A highly selective rasorber based on second-order resonance," *IEEE Antennas and Wireless Propagation Letters*, Vol. 19, No. 2, 223–227, Feb. 2020.

[8] Zargar, M. M., A. Rajput, K. Saurav, and S. K. Koul, "Frequency-selective rasorber based on high-Q Minkowski fractal-shaped resonator for realizing a low radar cross-section radiating system," *IEEE Transactions on Electromagnetic Compatibility*, Vol. 64, No. 5, 1574–1584, Oct. 2022.

[9] Xing, Q., W. Wu, Y. Yan, X. Zhang, and N. Yuan, "Frequency-selective rasorber with two wide absorption bands and two transmission zeros," *Microwave and Optical Technology Letters*, Vol. 64, No. 9, 1529–1535, Sep. 2022.

[10] Huang, H., C. Hua, and Z. Shen, "Absorptive frequency-selective transmission structures based on hybrid FSS and absorber," *IEEE Transactions on Antennas and Propagation*, Vol. 70, No. 7, 5606–5613, Jul. 2022.

[11] Xiu, X., W. Che, Y. Han, and W. Yang, "Low-profile dual-polarization frequency-selective rasorbers based on simple-structure lossy cross-frame elements," *IEEE Antennas and Wireless Propagation Letters*, Vol. 17, No. 6, 1002–1005, Jun. 2018.

[12] Costa, F. and A. Monorchio, "A frequency selective radome with wideband absorbing properties," *IEEE Transactions on Antennas and Propagation*, Vol. 60, No. 6, 2740–2747, Jun. 2012.

[13] Xue, K. and H. Zhai, "A compact ultrawideband frequency selective rasorber with hybrid 2-D and 3-D structure," *IEEE Antennas and Wireless Propagation Letters*, Vol. 21, No. 9, 1872–1876, Jun. 2022.

[14] Shang, Y., Z. Shen, and S. Xiao, "Frequency-selective rasorber based on square-loop and cross-dipole arrays," *IEEE Transactions on Antennas and Propagation*, Vol. 62, No. 11, 5581–5589, Nov. 2014.

[15] Chen, Q., D. Sang, M. Guo, and Y. Fu, "Miniaturized frequency-selective rasorber with a wide transmission band using circular spiral resonator," *IEEE Transactions on Antennas and Propagation*, Vol. 67, No. 2, 1045–1052, Feb. 2019.

[16] Yang, Z., W. Jiang, Q. Huang, and T. Hong, "A 2.5-D miniaturized frequency-selective rasorber with a wide high-transmission passband," *IEEE Antennas and Wireless Propagation Letters*, Vol. 20, No. 7, 1140–1144, Jul. 2021.

[17] Jiang, H., S. Liao, R. Li, and Q. Xue, "Independently switchable rasorber with wide transmission and low-reflection bands under dual polarization," *IEEE Transactions on Microwave Theory and Techniques*, Vol. 72, No. 2, 863–877, Feb. 2024.

[18] Jiang, B., H. Hu, Y. Wu, B. Chen, S. Lei, and J. Tian, "A switchable ATA rasorber with polarization selectivity and high roll-off characteristics," *IEEE Antennas and Wireless Propagation Letters*, Vol. 22, No. 9, 2075–2079, Sep. 2023.

[19] Bakshi, S. C., D. Mitra, and S. Ghosh, "A frequency selective surface based reconfigurable rasorber with switchable transmission/reflection band," *IEEE Antennas and Wireless Propagation Letters*, Vol. 18, No. 1, 29–33, Jan. 2019.

[20] Tang, M., Q. Liu, D. Zhou, Q. Liu, Z. Yao, and C. Pan, "Miniaturised frequency selective surface-based rasorber with wideband two-sided absorption and switchable transmission/reflection band," *IET Microwaves, Antennas & Propagation*, Vol. 17, No. 4, 284–291, 2023.

[21] Li, R., H. Hu, J. Tian, B. Jiang, B. Chen, and S. Lei, "Switchable rasorber with high-order frequency selective surface for transmission bandwidth extension," *Microwave and Optical Technology Letters*, Vol. 63, No. 6, 1705–1711, Jun. 2021.

[22] Jacobsen, R. E., S. Arslanagić, and A. V. Lavrinenko, "Water-based devices for advanced control of electromagnetic waves," *Applied Physics Reviews*, Vol. 8, No. 4, 041304, Oct. 2021.

[23] Saifullah, Y., Y. He, A. Boag, G.-M. Yang, and F. Xu, "Recent progress in reconfigurable and intelligent metasurfaces: A comprehensive review of tuning mechanisms, hardware designs, and applications," *Advanced Science*, Vol. 9, No. 33, 2203747, 2022.

[24] Shao, L. and W. Zhu, "Electrically reconfigurable microwave metasurfaces with active lumped elements: A mini review," *Frontiers in Materials*, Vol. 8, 689665, Jun. 2021.

[25] Liao, K., S. Liu, X. Shao, X. Zhang, X. Zheng, and X. Kong, "An ultra-wideband dual-band hybrid frequency-selective rasorber," *International Journal of RF and Microwave Computer-Aided Engineering*, Vol. 32, No. 7, e23197, 2022.

[26] Jiang, H., S. Liao, R. Li, and Q. Xue, "Independently switchable rasorber with wide transmission and low-reflection bands under dual polarization," *IEEE Transactions on Microwave Theory and Techniques*, Vol. 72, No. 2, 863–877, Feb. 2024.

[27] Yang, Z., W. Jiang, Q. Huang, and T. Hong, "A 2.5-D miniaturized frequency-selective rasorber with a wide high-transmission passband," *IEEE Antennas and Wireless Propagation Letters*, Vol. 20, No. 7, 1140–1144, Jul. 2021.

[28] Zhao, M., H. Li, Z. Wu, B. Wang, X. Min, and Q. Cao, "Wideband second-order bandpass frequency selective surface with high selectivity," *Microwave and Optical Technology Letters*, Vol. 65, No. 8, 2230–2237, 2023.

[29] Xue, K. and H. Zhai, "A compact ultrawideband frequency selective rasorber with hybrid 2-D and 3-D structure," *IEEE Antennas and Wireless Propagation Letters*, Vol. 21, No. 9, 1872–1876, 2022.

[30] Shen, Z., N. Kou, S. Yu, Z. Ding, and Z. Zhang, "Miniaturized frequency selective rasorber based on meander-lines loaded lumped resistors and a coupled resonator spatial filter," *Progress In Electromagnetics Research M*, Vol. 90, 147–155, 2020.

[31] Li, R., J. Tian, B. Jiang, Z. Lin, B. Chen, and H. Hu, "A switchable frequency selective rasorber with wide passband," *IEEE Antennas and Wireless Propagation Letters*, Vol. 20, No. 8, 1567–1571, Aug. 2021.

[32] Ge, J., W. Jiang, T. Hong, Y. Gao, and S. Gong, "Bandpass frequency-selective rasorber with wide transmission band and high selectivity based on multiorder resonance," *IEEE Transactions on Antennas and Propagation*, Vol. 71, No. 12, 9621–9632, Dec. 2023.